A Flexible Infrastructure for Dynamic Power Control of Electric Vehicle Battery Chargers

Vítor Monteiro, *Student Member, IEEE*, João Paulo Carmo,
J. G. Pinto, *Member, IEEE*, and João Luiz Afonso, *Member, IEEE*

***Abstract*—This paper proposes a flexible infrastructure for dynamic power control (FIDPC) of electric vehicle (EV) battery chargers. This infrastructure dynamically adjusts the EV battery charger current, according to the power demand of the home wherein the vehicle is plugged. An infrastructure was implemented to validate this proposal. This infrastructure is composed by an EV battery charger and a communication system based on a radio-frequency (RF) interface. The battery charger has nominal power of 3.6 kVA and operates with sinusoidal current and unitary total power factor, whereas the RF interface provides continuous data flow to the battery charger with information on the home total current consumption (root-mean-square value). Experimental tests were performed under realistic conditions to validate the concept behind the proposed FIDPC. These tests served to assess the behavior of the EV battery charger with dynamic power control on a single-phase 230-V 16-A 50-Hz residential electrical installation. The experimental results confirm the quick time response of the FIDPC, even when working under heavy-home-load variations.**

***Index Terms*—Electric vehicles (EVs), home-to-vehicle (H2V), power quality, radio-frequency (RF) communication, smart grids, vehicle-to-grid (V2G).**

I. Introduction

ELECTRIC mobility represents a new paradigm for the transportation sector [1], [2]. This includes the use of hybrid electric vehicles and electric vehicles (EVs), which can be combined with renewable energy [3], [4] and simultaneously integrated into the future smart grids [5]. Nevertheless, the integration of EVs into smart grids will be strongly dependent on major technological issues. Few of these issues include the innovation in energy storage systems [6], battery charging strategies [7], and communications field [8]. However, deregulated proliferation of EVs can cause power quality problems in the power grid [9]. On the other hand, regulated proliferation can result in benefits to the EV driver and to power grid management [10], [11]. An example of such benefits can be observed in [12], where a control strategy for charging the batteries of EVs, considering the charging schedule uncertainty and the energy price variation, is proposed. These benefits are mainly related with the bidirectional power flow and exchanged data between the power grid and the EV battery charger [13]. It must be noted that if the EV battery charger is bidirectional, it can consume or supply energy from or to the power grid, respectively. Thereby, apart from the battery charging process (i.e., grid-to-vehicle (G2V) mode), part of the energy previously stored in the batteries can be delivered back toward the power grid (i.e., vehicle-to-grid (V2G) mode) [14]. The V2G operation mode must take into account the power grid requirements and the benefits to the EV driver. This operation considers few critical issues, e.g., the price of energy to sell or to buy and the battery state-of-charge (SoC). The main advantages behind the V2G operation mode are related with load shedding, ancillary services, and electric utility [15]–[17]. Additionally, the interactivity of EVs with smart grids will demand efforts related to the development of smart homes [18]. Thus, an increase in the research and development of home-to-vehicle (H2V) technologies for application in smart homes, to allow for the implementation of energy management and efficiency solutions [19], [20], is expected. In this context, smart homes are facing decision-making problems, requiring the best possible decision toward the integration of smart devices in a hierarchical architecture in the smart-grid context without neglecting power grid stability and quality-of-service [21], [22]. The development of these kinds of technologies for EVs is more pertinent for research, with knowledge that private vehicles are parked, on average, 95% of the time [23] and that, at the same time, a significant majority of them are parked at home between 8:00 P.M. and 7:00 A.M. [24]. In most cases, the battery charging process is performed during this period of the day, in which the EV represents an extra residential load during this period. For example, it is during this period that a significant number of domestic apparatus (TVs, lights, washing machines, and so on) are turned on and off according to user preferences. The monitoring of the EV battery charging process is not the only advantage brought by the smart-home concept. In fact, there are other advantages, where the most important is that associated with the possibility of the EVs interacting with the home. Therefore, the main contribution of this paper is a flexible infrastructure for a dynamic control of the EV battery charging process, according to the current required by the home loads. Nevertheless, another important contribution is the controlled operation as V2G in the smart-home context,

Manuscript received March 18, 2014; revised December 16, 2014 and April 16, 2015; accepted August 31, 2015. Date of publication September 11, 2015; date of current version June 16, 2016. This work was supported by the Fundação para a Ciência e Tecnologia (FCT) through Project PEst-UID/CEC/00319/2013. The work of V. Monteiro was supported by the FCT agency through a doctoral scholarship under Grant SFRH/BD/80155/2011. The review of this paper was coordinated by Dr. D. Cao.

V. Monteiro, J. G. Pinto, and J. L. Afonso are with the Department of Industrial Electronics, Centro Algoritmi, University of Minho, 4800-058 Guimarães, Portugal (e-mail: vmonteiro@dei.uminho.pt; gpinto@dei.uminho.pt; jla@dei.uminho.pt).

J. P. Carmo is with the Department of Electrical Engineering (SEL), University of São Paulo (USP), 13566-590 São Paulo, Brazil (e-mail: jcarmo@sc.usp.br).

Color versions of one or more of the figures in this paper are available online at http://ieeexplore.ieee.org.

Digital Object Identifier 10.1109/TVT.2015.2478151

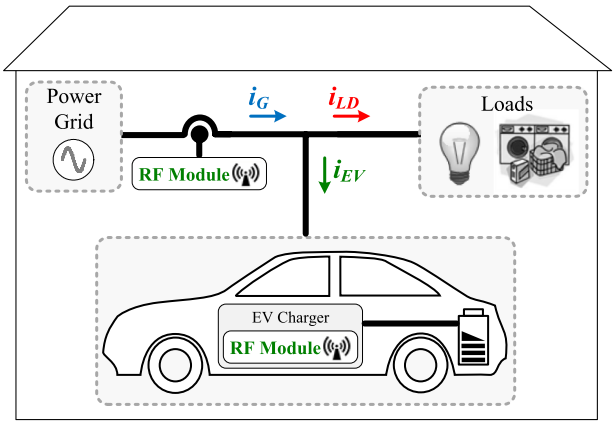

Fig. 1. System architecture of the proposed FIDPC of EV battery chargers.

which contributes in avoiding trips in the main circuit breaker when the home current exceeds the maximum allowed value. The context of these contributions is illustrated by the system architecture presented in Fig. 1, where i_G represents the grid current, i_{LD} is the home-load current, and $i_{\rm EV}$ is the EV battery charger current. As shown in the system architecture, the EV battery charger current is dynamically adjusted according to the changes in the totality of the home-load current. This dynamic adjustment is a key contribution in maintaining the grid current with a constant root mean square (RMS) value. Moreover, the EV battery charger current can be adjusted in both H2V and V2G operation modes without neglecting the power quality.

A data communication solution for sending the RMS value of the current measured in the home toward the EV battery charger is a key point to achieve the aforementioned goal. For such purpose, there are a few options of communication systems available for providing reliable data between the electrical switchboard inside the home and the EV battery charger, such as radio frequency (RF), power line communication, and Wi-Fi. The RF-based solution was selected due to its intrinsic simplicity of implementation, adaptation to different scenarios, independence of Internet communication, low prototyping time, and, most importantly, low cost in implementation [25]. In this context, this paper presents a flexible infrastructure for dynamic power control (FIDPC) supported on RF communication for achieving a controllable EV battery charging process. As shown in Fig. 1, the RF transmitter is installed in the home electrical switchboard, whereas the RF receiver is installed in the EV battery charger. This FIDPC was experimentally validated with the help of a prototype particularly developed for such purpose. Despite the proposed FIDPC having been idealized and experimentally validated in a home scenario, it is important to note that it can also be integrated in the future smart grids to allow adjusting the EV battery charging process.

The remainder of this paper is organized as follows. The H2V and V2G operation modes are presented in Section II, whereas Section III presents a case study and a simulation analysis. Section IV presents the system implementation, describes the control algorithms, and details the proposed EV battery charger hardware and the communication system. The experimental results in steady state and in transient response are presented and discussed in Section V. Finally, the conclusions are presented in Section VI.

II. System Architecture

Fig. 1 shows the system architecture of the proposed FIDPC, which is composed of the home electrical switchboard, including the supporting RF module (transmitter) and the EV battery charger (where the RF receiver is installed). This infrastructure is designed to operate in accordance with H2V and V2G technologies. The EV battery charger can recharge the EV battery when the H2V mode is selected. Alternatively, the energy can flow in the reverse direction when the V2G mode is selected, i.e., the energy stored in the batteries can be delivered to the power grid. The EV battery charger operates with a sinusoidal current waveform in the ac side for both H2V and V2G operation modes, contributing to the power quality in electrical power grids. The architecture of the FIDPC proposed in this paper intends to adjust the EV battery charger current $(i_{\rm EV})$ as function of the current required by the other electrical loads inside the home (i_{LD}). Hence, the control of the EV battery charger current $(i_{\rm EV})$ is performed in its digital control system according to the home current (i_G) provided by the RF module installed in the electrical switchboard. This contribution is important when considering that, nowadays, the common situation is to have the energy flowing from the power grid toward the loads of the home with no any control and simply limited by the contracted power for the home. The implementation of this control strategy by the FIPDC avoids electrical switchboard overload.

A. H2V Operation Mode

In the H2V operation mode, the power flows from the power grid to the EV battery charger. The charging power of the EV battery charger is a function of the power demand profile inside the home and is established that the maximum consumed power in the EV battery charger corresponds to the power contracted with the electricity service provider. The electricity service provider installs a circuit breaker rated to the nominal current to guarantee that the contracted power is never exceeded. Therefore, the circuit breaker trips every time the home current exceeds the limit during a short period of time. This is why the current is the variable to be measured and tracked. This is done by measuring the RMS value of the home current, followed by its transmission to the EV battery charger. A current sensor, a microcontroller, and an RF communication module are used in the execution of these procedures (i.e., current measurement and data transmission). The flowchart in Fig. 2 shows the control algorithm during the H2V operation mode. In this mode, the current is measured through a current sensor installed inside the home electrical switchboard. The current signal is sampled at the frequency $f_s = 1.6$ kHz to acquire 32 samples of the instantaneous current per 50-Hz cycle. This minimum number of samples is intended to reduce the effect of time discretization and, thus, to obtain a reliable measure of the RMS value. This minimum number of samples is in accordance with the International Standard IEC 62053-21.

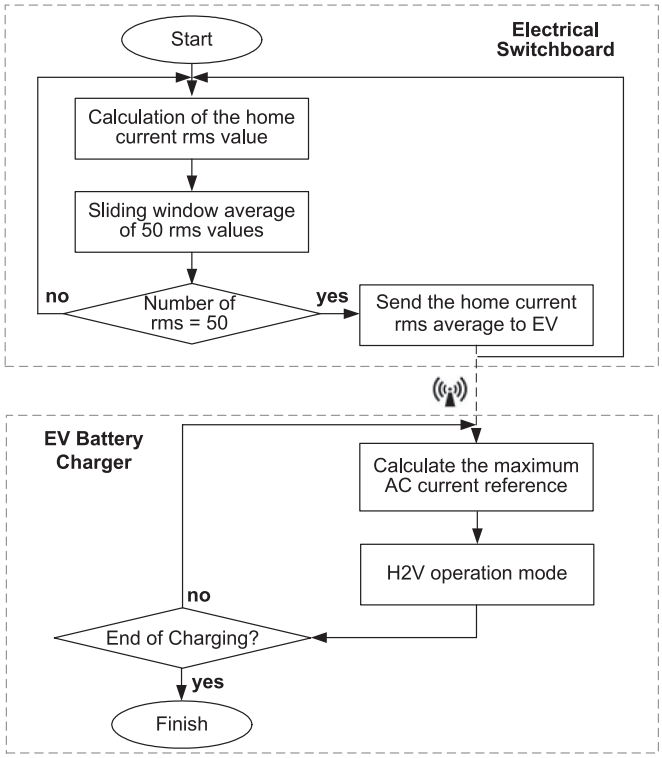

Fig. 2. Control algorithm of the proposed FIDPC architecture during the H2V operation mode.

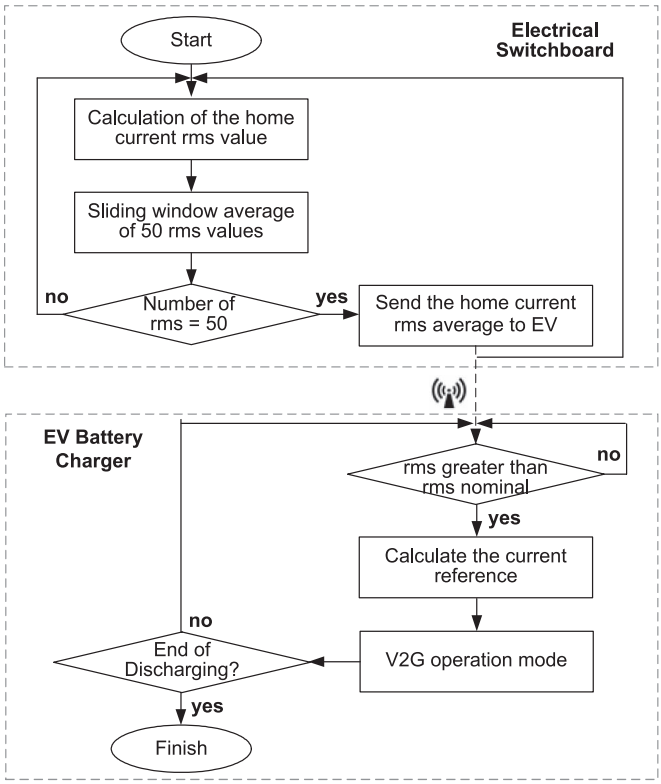

Fig. 3. Control algorithm of the proposed FIDPC architecture during the V2G operation mode.

It must be noted that the RMS value of the current is calculated for each 50-Hz cycle.

B. V2G Operation Mode

During the V2G operation mode, the energy flows from the EV battery charger toward the power grid. The V2G operation mode can also be used to avoid the circuit breaker trip, i.e., when the EV is plugged in but not charging and the home loads exceed the nominal power contracted with the service provider, the EV can deliver part of the energy stored in the batteries back to the power grid to avoid the circuit breaker trip. In this operation mode, the RF communication also represents an asset to the future smart grids, to receive control commands defining its operation. Due to the absence of smart grids controlling this operation, the values used in the experimental tests are predefined in the digital controller.

The flowchart in Fig. 3 shows the control algorithm behind the V2G operation mode. Despite the benefits of this operation mode, special care must be taken due to a few restrictions. The main restrictions are associated with both the battery SoC and the compromise assumed between the EV owner and the power grid service provider. It is interesting to note that this operation mode finds additional advantages in smart-grid scenarios, either in reactive power compensation [26], or through an aggregator to regulate the power grid frequency [27], or both.

III. Case Study and Simulation Analysis

To illustrate the benefits of the proposed FIDPC, the battery charging of the EV *Renault Fluence* [28] was monitored. This process was monitored several times in different conditions (e.g., performing the battery charging process after full discharge and with different ambient temperatures), using a *Yokogawa DL708E* digital oscilloscope and a *FLUKE 435* power quality analyzer. Fig. 4 shows the circuit breaker trip that occurred during the EV *Renault Fluence* battery charging process due to an overcurrent caused by the home-load current

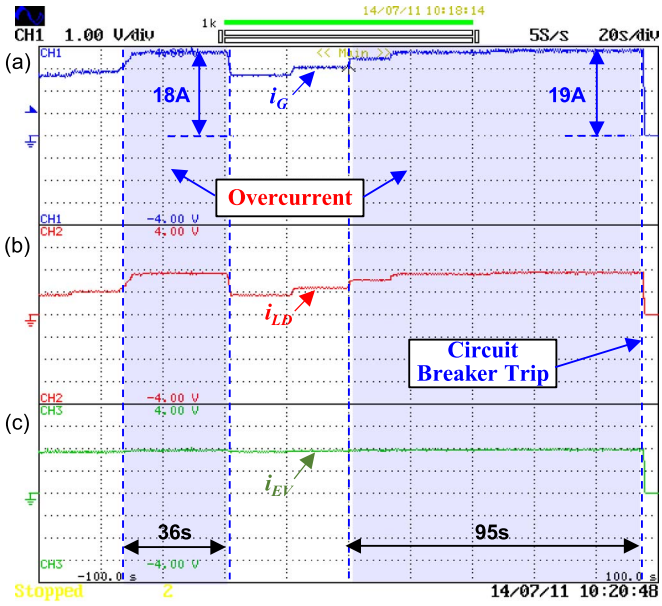

Fig. 4. Example of circuit breaker trip caused by overcurrent during the charge of the EV *Renault Fluence*. (a) Grid current (i_G—5 A/div). (b) Home-load current (i_{LD}—5 A/div). (c) EV battery charger current (i_{EV}—5 A/div).

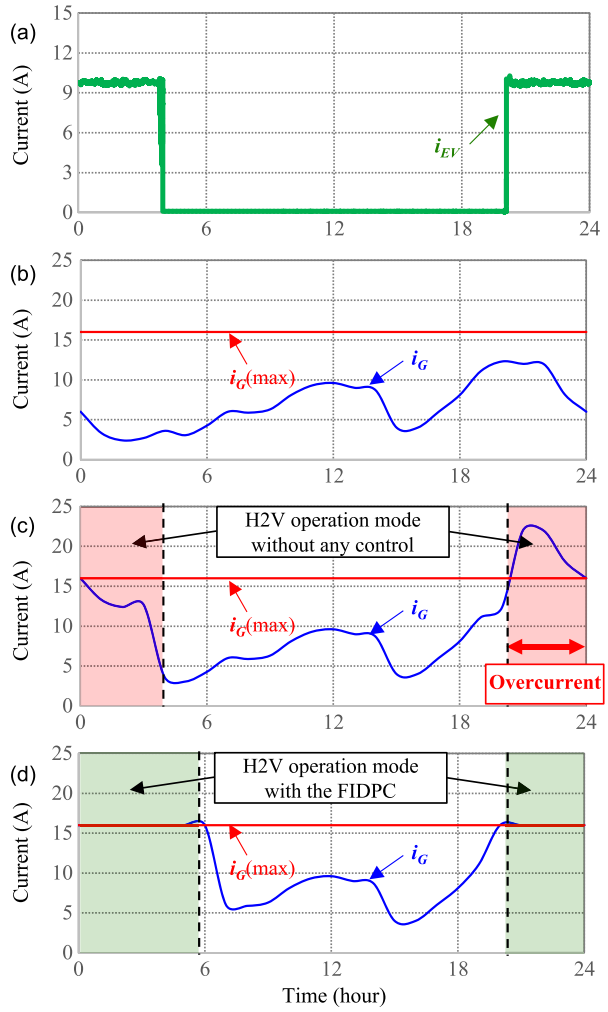

Fig. 5. Comparison results of an EV *Renault Fluence* charging scenario with and without the proposed FIDPC. (a) EV *Renault Fluence* charging current profile. (b) Typical daily home-load current. (c) H2V operation mode without control. (d) H2V operation mode with the proposed FIDPC.

variation. In this figure, the grid current (i_G), the home-load current (i_{LD}), and the EV battery charger current $(i_{\rm EV})$ are shown. As shown, before the circuit breaker trip, two periods of overcurrent occurred. In the first period of 36 s, the maximum current was 18 A, and in the second period of 95 s, the maximum current was 19 A.

Based on this situation and considering the charging profile of the EV *Renault Fluence*, a computer simulation (see Fig. 5) to illustrate the benefits of the FIDPC strategy was performed. In this simulation, it was considered that the EV *Renault Fluence* battery charging process starts at 8:00 P.M. Fig. 5(a) shows the RMS values of the main current of the EV *Renault Fluence* during typical charging, with the batteries initially fully discharged. These values were registered with the *FLUKE 435* and used in the computer simulation. It is important to note that for obtaining these values, it was necessary to disconnect some home loads. In this case, the EV battery charging process started at 8:00 P.M. and finished at 4:00 A.M., i.e., with a total time of 8 h. As shown, the current was maintained constant and equal to 10 A almost all the time. The exception to this was observed only in the last 10 min, when the current was not constant. It is also important to note that the total power factor (TPF) was maintained almost unitary (TPF $= 0.99$) during the entire EV battery charging process, and the current was kept almost sinusoidal, with a percentage of total harmonic distortion ($\rm THD_i\%$) of about 5%.

Based on the EV *Renault Fluence* battery charging profile and considering the typical home-load profile represented in Fig. 5(b) (also monitored using *FLUKE 435*), two distinct situations were simulated. As represented in Fig. 5(b)–(d), it was assumed that the maximum accepted RMS value of current is 16 A, which corresponds to the rated current of the main circuit breaker of the home electrical installation. Fig. 5(c) shows the first simulation, without the FIDPC strategy and without disconnecting any home loads. As can be observed in this hypothetical situation, the maximum current of the main circuit breaker is exceeded in 4 h, and the battery charging process cannot be performed in practice. Fig. 5(d) shows the second simulation, with the FIDPC strategy and without disconnecting any home loads. As can be observed, with the FIDPC working, the EV battery charging current was controlled, and the charging time is extended until 6:00 A.M. In this case, due to the action of the FIDPC, the home current was maintained below the circuit breaker rate, and therefore, trips were avoided. Although these results portrayed a specific case, they are quite representative of the EV battery charging process at homes.

Additionally, the proposed FIDPC makes possible the delivery, in a controlled way, of part of the stored energy in the batteries to the power grid (e.g., working in the V2G operation mode). In a smart-grid scenario, this operation mode will be controlled by a Collaborative Broker [29]. The H2V and V2G operation modes are carefully described further to complement this analysis.

The charging process of lithium batteries is usually performed in two stages to accomplish most of the manufacturers' recommendations: constant current followed by constant voltage [30], [31]. In the first stage, the batteries are charged with constant dc current until the dc voltage reaches the maximum value recommended by the manufacturer. At the end of this stage, the batteries are charged to about 80% of their capacity. Then, during the second stage, the battery charger output voltage is maintained constant until the current approaches zero. This point represents the end of the charging process. The EV battery charger used in this work was designed to follow this strategy and to comply with the recommendations of the manufacturers by controlling the charging current during the first stage and the charging voltage during the second stage. As stated previously, it is mandatory to respect the maximum allowable current of the main circuit breaker to avoid trips. This can be done by adjusting the charging current (i_{BAT}) and voltage (v_{BAT}) in the batteries (on the dc side of the EV battery charger) to control the ac current $(i_{\rm EV})$ of the EV battery charger (on the power grid side). This strategy influences the time required to complete a full charge. This influence in the charging time is the price to pay for ensuring that the home electrical energy is never interrupted. Moreover, the EV battery charger predicts an additional safety mechanism to the batteries by keeping these variables (dc charging current and voltage) within the battery manufacturer recommendations.

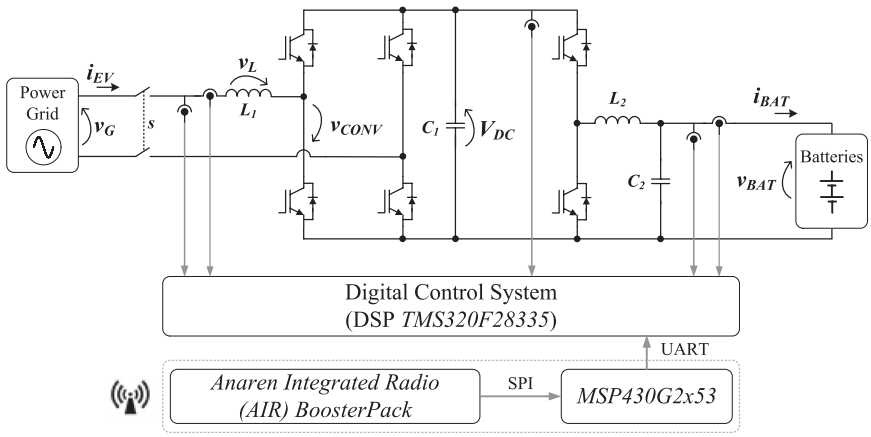

Fig. 6. Electric diagram of the EV battery charger and respective RF link.

TABLE I
EV BATTERY CHARGER SPECIFICATIONS

Parameters	Value	Unit
Input ac Voltage	230 ± 10%	V
ac Frequency	50 ± 1%	Hz
Maximum Input ac Current	16	A
Input ac Current Ripple	0.5	A
Maximum Input Power	3.6	kVA
Total Power Factor @ Full Load	0.99	
THD_i @ Full Load	< 3%	
Battery Voltage Range	270-360	V
Maximum Battery Charging Current	10	A
Efficiency	> 90%	
Dimensions	250×290×95	mm

IV. SYSTEM IMPLEMENTATION

Fig. 6 shows the electric diagram of the EV battery charger equipped with an RF communication system. In the system implementation, two RF modules are used. The first is integrated with the home electrical switchboard to serve as a transmitter and, therefore, to send wirelessly the information of the current into the EV battery charger. The second is a piece of hardware, which is an integral part of the EV battery charger, to operate as a receiver. This hardware is specifically dedicated to meet the aforementioned approaches. The switch s is used to connect/disconnect the EV battery charger to/from the power grid. The EV battery charger autodisconnects from the power grid in case of voltage sags or swells.

A compromise between cost, size, and efficiency was taken into account during the design of the EV battery charger, to define the specifications and requirements of the electronic components. This compromise aims for the design of a reliable EV battery charger prototype that will be tested in an EV prototype designed by a national company. Table I lists the design specifications of the EV battery charger.

A. Control Algorithms

Using the proposed strategy to adjust the current of the EV battery charger can result in the occurrence of oscillations in the home current. In this context, two strategies are possible for overcoming this problem and, thus, for avoiding the oscillations. In the first strategy, the RMS values of the home current are transmitted at a 20-ms fixed rate (time necessary to calculate the one-cycle RMS value). Therefore, this allows for modifying the reference current of the EV battery charger when sudden variations in the RMS value of the home current are present. The digital implementation that allows the calculation of the RMS value is given by

$$I_G[k] = \sqrt{\frac{1}{N}\sum_{k=1}^{k=N} i_g^2[k]} \tag{1}$$

where N is the number of samples in each cycle of the power grid voltage, and k denotes the actual sample.

In the second strategy, an alternative methodology to the transmission of the one-cycle RMS value is followed by considering an average of M RMS values. These M RMS values are obtained by a sliding-window average across the one-cycle RMS values. The digital implementation of the sliding sum used in the sliding window is calculated as follows:

$$sum[k] = sum[k-1] - I_g^2[k-M] + I_g^2[k]. \tag{2}$$

Additionally, the average of the RMS values $(I_{G\_AVG}[k])$ of the grid current is calculated using

$$I_{G\_AVG}[k] = \sqrt{\frac{sum[k]}{M}}. \tag{3}$$

The FIDPC proposed in this paper uses the second strategy to adjust the reference current to the EV battery charger. The sliding window uses $M = 50$ one-cycle RMS values. After the calculation, the average of the RMS values is transmitted. Each transmitted average value is coded with 8 bits, resulting in a quantization error of 0.125 A, for a maximum of 16-A power grid current. Additionally, the EV battery charger applies a margin of slack to compensate for these rounding and small

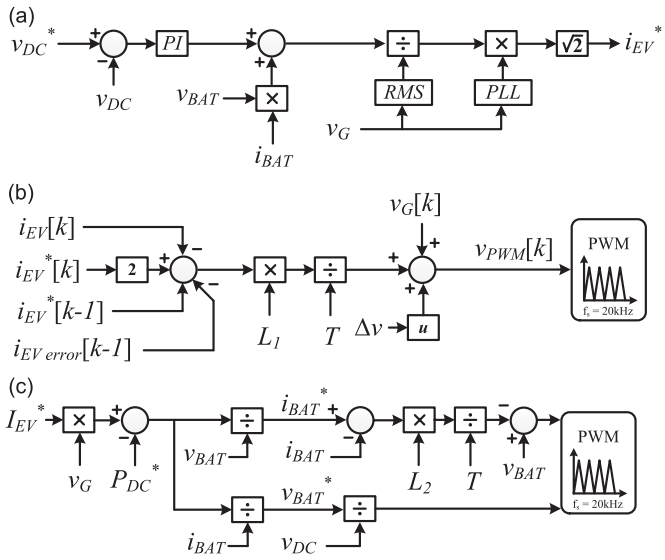

Fig. 7. Control block diagram of the EV battery charger. (a) DC-link voltage control and EV battery charger current reference. (b) Current control technique and unipolar pulsewidth modulation (PWM) modulator. (c) Battery current or voltage control.

load variances inside the home. The FIDPC uses an RF link at 868 MHz to transmit the average of the RMS values from the electrical switchboard toward the EV battery charger. This carrier frequency belongs to the Industrial, Scientific and Medical (ISM) band that was selected due to the following issues: the commercial availability at a large scale of RF modules and its freedom of usage without the need for a specific license of operation.

Fig. 7 presents the control block diagram of the EV battery charger. Fig. 7(a) shows the control diagram that allows the adjustment of the reference current for performing the EV battery charging process as a function of the RMS current required by the loads at home. The dc-link voltage $(v_{\rm DC})$ is adjusted to their voltage reference $(v^*_{\rm DC})$ through a controller programmed for a proportional and integral action. The power reference $(P^*_{\rm DC})$ is then obtained as

$$P^*_{\rm DC} = k_p\left(v^*_{\rm DC} - v_{\rm DC}\right) + k_i \int \left(v^*_{\rm DC} - v_{\rm DC}\right) dt. \quad (4)$$

The power on the dc side to charge the batteries is expressed as

$$P^*_{BAT} = i_{BAT} v_{BAT} \quad (5)$$

and the active power reference for the ac side is expressed as

$$P^* = P^*_{BAT} + P^*_{\rm DC}. \quad (6)$$

The RMS value of the reference current $(I^*_{\rm EV})$ of the EV battery charger is calculated as

$$I^*_{\rm EV} = \frac{P^*}{V_G} \quad (7)$$

where V_G is the RMS value of the power grid voltage. The RMS value of the reference current $(I^*_{\rm EV})$ is a function of the instantaneous reference current (i^*_{BAT}) and voltage (v^*_{BAT}) to charge the batteries. The instantaneous reference current $(i^*_{\rm EV})$ must be in phase with the fundamental component of the power grid voltage (v_G). This is achieved by multiplying that quantity by a reference signal pll, whose amplitude is unitary. This reference signal (pll) is obtained from a phase-locked loop [32]. Then, the reference current is affected by the gain of $\sqrt{2}$ as follows:

$$i^*_{\rm EV} = \sqrt{2}\, I^*_{\rm EV} pll. \quad (8)$$

As shown in Fig. 7(b), the synthesizing of the instantaneous reference current $(i^*_{\rm EV})$ is done with the help of a current control strategy, as described in [33]. Fig. 6 allows for establishing the following equation:

$$v_G = v_L + v_{CONV} \quad (9)$$

where v_L is the inductance voltage, and v_{CONV} is the voltage produced by the bidirectional converter. The instantaneous current error $(i_{{\rm EV}error})$ is a function of the instantaneous current reference $(i^*_{\rm EV})$ and the instantaneous current measured $(i_{\rm EV})$. The expression of $i_{{\rm EV}error}$ is given as

$$i_{{\rm EV}error} = i^*_{\rm EV} - i_{\rm EV}. \quad (10)$$

Equation (9) can be rewritten in terms of (10), resulting in

$$v_{CONV} = -L_1 \frac{di^*_{\rm EV}}{dt} + L_1 \frac{di_{{\rm EV}error}}{dt} + v_G. \quad (11)$$

The high sampling frequency (40 kHz) used allows for the approximation of the two derivatives in (11) by functions with linear variation. Thus, the voltage (v_{CONV}) produced by the converter can be expressed in terms of the discrete samples as

$$v_{CONV}[k] = v_G[k] - \frac{L_1}{T}\left(2i^*_{\rm EV}[k] - i^*_{\rm EV}[k-1] - i_{\rm EV}[k] - i_{{\rm EV}error}[k-1]\right) \quad (12)$$

where T is the sampling period. Then, the gate pulse patterns are obtained through a unipolar sinusoidal PWM strategy with a 20-kHz center-aligned triangular carrier. To mitigate the deadtime effect, a strategy was used, which consists of adding a constant value (Δv) to the voltage reference (v_{CONV}) during the positive semicycle and subtracting the same value during the negative semicycle, i.e.,

$$v^*_{\rm PWM}[k] = v_{CONV}[k] + u\Delta v \quad (13)$$

where Δv is the voltage to compensate for the deadtime effect, and u assumes one of these following values:

$$u = \begin{cases} 1, & i^*_{\rm EV} > 0 \\ -1, & i^*_{\rm EV} < 0. \end{cases} \quad (14)$$

Fig. 7(c) shows the block diagram of the battery current and voltage control. To control the charging current, the dc–dc converter must produce the voltage $(v^*_{\rm PWM\_DC})$, according to

$$v^*_{\rm PWM\_DC}[k] = v_{BAT}[k] + \frac{L_2}{T}\left(i^*_{BAT}[k] - i_{BAT}[k]\right). \quad (15)$$

On the other hand, the process to control the charging voltage directly affects the duty cycle (δ) in the dc–dc converter as follows:

$$\delta[k] = \frac{v^*_{BAT}[k]}{v_{\rm DC}[k]}. \tag{16}$$

Additionally, it must be noted that the frequency of 20 kHz is selected for the triangular carrier in the PWM of the dc–dc converter.

B. EV Battery Charger Hardware

The implemented 3.6-kVA EV battery charger is composed of two bidirectional power converters: an ac–dc converter and a dc–dc converter. In both converters, insulated-gate bipolar transistors (IGBTs; model *FGA25N120ANTD*) are used, i.e., four in the bidirectional ac–dc converter and two in the reversible dc–dc converter. A snubber capacitor (with 0.1 μF/1000 V) is placed parallel to each leg to minimize the voltage stress across the semiconductors. Each leg of the ac–dc converter operates with a 20-kHz switching frequency (unipolar PWM), resulting in a frequency (f_s) in the coupling inductance of 40 kHz. An inductor of 5 mH is used for obtaining a maximum ac current ripple $(\Delta i_{\rm EV})$ of 0.5 A. This value is obtained according to

$$\Delta i_{\rm EV} = \frac{v_{\rm DC}}{8\, L_1 f_s}. \tag{17}$$

A capacitor of 2.7 mF is used to maintain the oscillation in the dc-link voltage below 10 V. This value is obtained according to

$$\Delta v_{\rm DC} = \frac{2\, V_G I_{\rm EV}}{\omega\, C_1 V_{\rm DC}}. \tag{18}$$

The L_2C_2 filter is connected to the output of the dc–dc converter for keeping the maximum output voltage ripple below 0.1 V. The selected elements for this filter are an inductor of 300 μH and a capacitor of 680 μF. The calculation of these elements is given in the following equation:

$$L_2C_2 = \frac{(v_{\rm DC} - v_{BAT})v_{BAT}}{8\, f_s^2 v_{\rm DC}\Delta v_{BAT}}. \tag{19}$$

Table II lists the main components that are used in the EV battery charger prototype. The topology that is used in the EV battery charger design imposes sinusoidal current on the ac side during both H2V and V2G modes. The control system for implementing the H2V/V2G algorithms is composed of several electronic circuits with analog and digital signals. The algorithms in the digital control system are implemented in a digital signal processor (DSP) *TMS320F28335* (from *Texas Instruments*). This DSP contains two internal analog-to-digital converters (ADCs) with eight channels each. These ADCs receive both voltage and current signals that are provided by the signal conditioning circuit. The voltage and current signals of the bidirectional power converter are obtained through Hall-effect sensors (from the *LEM* manufacturer) in the signal conditioning circuit. An offset must be added to all the bipolar signals (including the current i_{BAT}) because the ADCs are unipolar. A circuit is also used to provide protection against overvoltages and overcurrents on both sides of the power converters. It must be noted that transient voltage surge suppressors are also used to protect the EV battery charger against lightning. The control signals to the IGBT drivers are provided by the command circuit, which receives the control signals from the DSP. Currently, the operation of the EV battery charger occurs in accordance with the orders given by the user through the external interface. Additionally, the EV battery charger is prepared for future functionalities. One of these added functionalities is, for example, the possibility of being controlled by a Collaborative Broker in smart grids, which is defined when the EV battery charger works either as H2V or as V2G. Fig. 8 shows the setup used to obtain the experimental results. More specifically, Fig. 8(a) shows the final aspect of the developed EV battery charger, whereas Fig. 8(b) shows the RF communication system that is implemented in the home electrical switchboard. Fig. 8(c) shows the whole tested system.

TABLE II
MAIN COMPONENTS SELECTED TO THE BATTERY CHARGER

Component	Model / Value	Quantity
DSP	*TMS320F28335*	1
IGBT	*FGA25N120ANTD*	6
IGBT Drivers	*HCPL3120*	6
Snubber Capacitor	1 µF / 1000 V	3
Inductor L_1	5 mH / 16 A	1
Capacitor C_1	680 µF / 450 V	4
Inductor L_2	300 µH / 15 A	1
Capacitor C_2	680 µF / 450 V	1
Current Sensor	LA 55-P	2
Voltage Sensor	LV 25-P	3

C. Communication System

An *Anaren Integrated Radio* (AIR) *BoosterPack* module is used to integrate the core elements that compose the FIDPC. More specifically, the AIR module is used to establish the RF connectivity between the home electrical switchboard and the EV battery charger. Such communication module is composed by the on-board *A110LR09A* radio module that integrates an antenna to operate in the European 868-MHz ISM band and by the *Texas Instruments CC110L* transceiver. The AIR *BoosterPack* is a low-power wireless transceiver extension module.

In the EV battery charger, the AIR *BoosterPack* exchanges data with a microcontroller model *MSP430G2x53* through a serial peripheral interface (SPI). This microcontroller exchanges data with the DSP through a universal asynchronous receiver/transmitter interface. In the home's electrical switchboard, the AIR *BoosterPack* establishes communication with the *MSP430G2x53* (microcontroller from *Texas Instruments*) through an SPI interface.

The home-load current is measured through a current sensor model *LTSR 15 NP* from the *LEM* manufacturer. This current is then adjusted through a signal conditioning circuit, and its

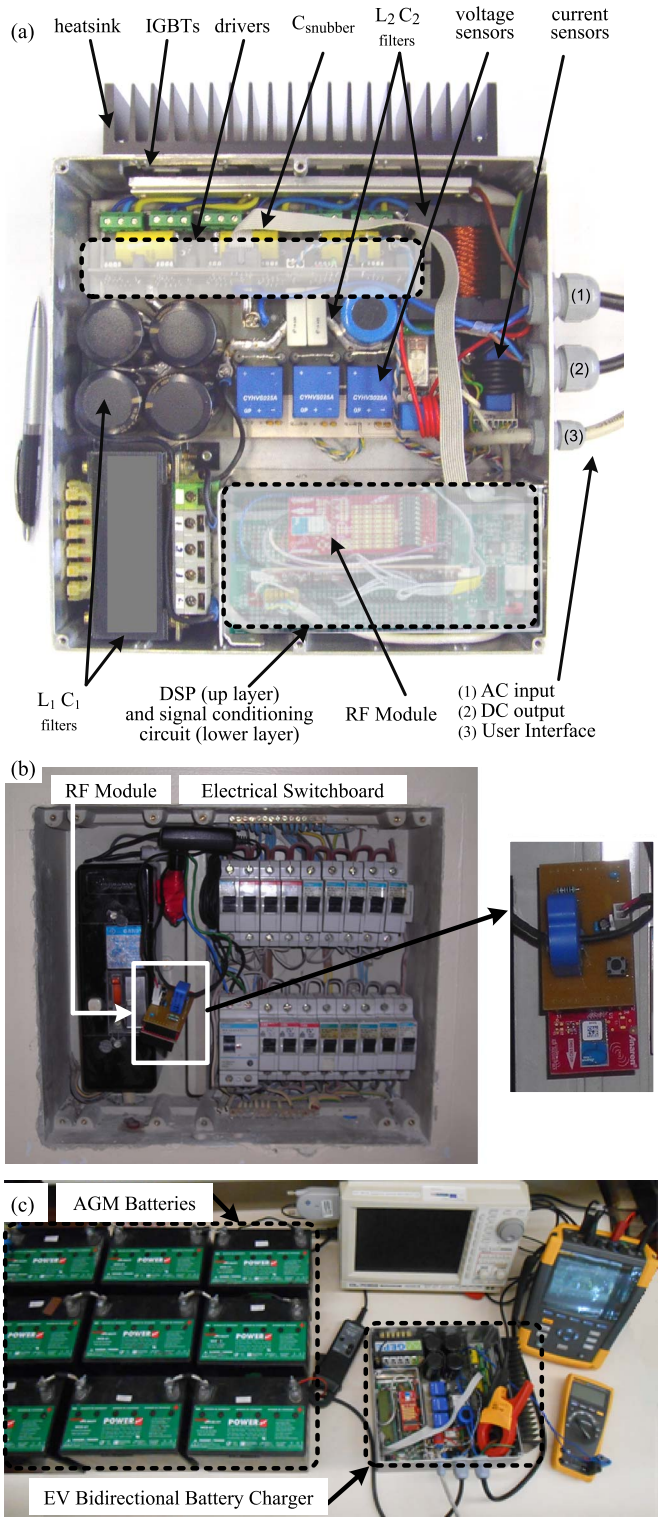

Fig. 8. Setup used to obtain the experimental results. (a) Developed EV battery charger. (b) RF communication system implemented in the home electrical switchboard. (c) Workbench of the tested system.

value is further acquired by the *MSP430G2x53* microcontroller through an ADC channel at a fixed sampling rate. Finally, the sliding average of 50 RMS values is calculated and sent toward the EV battery charger to adjust the setpoints of the EV battery charging process.

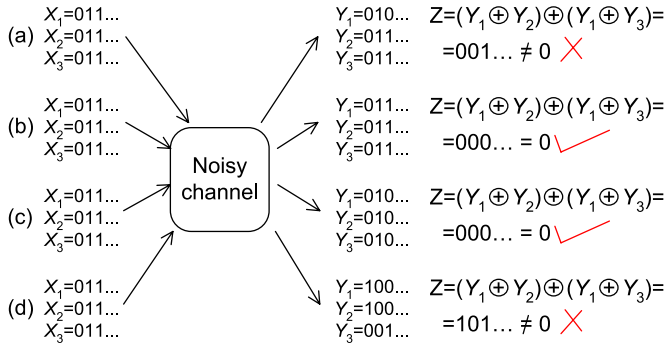

Fig. 9. Representation of four examples of the transmission and reception of four RMS values.

The AIR *BoosterPack* module is used to transmit the RMS value of the home-load current to the EV battery charger. The digital data acquired with the ADC (10 bits) of the *MSP430G2x53* are converted into an RMS value (as previously explained) and further coded and transmitted as a single character of 8 bits. Each data character is transmitted three times to allow the receiver to detect errors and to take preventive actions with its relation. This means that to transmit a single RMS value effectively, a transmission of three characters is required. The data characters are received, analyzed, and obtained by the EV battery charger, and then, the corresponding RMS value for the ac side of the EV battery charger (i^*_{EV}) is determined and used in the H2V (or V2G) algorithms. Fig. 9 shows four examples of the transmission and reception of a few RMS values. The label $X1$ corresponds to the binary representation of the main character, whereas the labels $X2$ and $X3$ correspond to the binary representation of the two characters that will allow the possible error detection. During normal operation, the errors are not present; therefore, on the receiver's side $Y1 = Y2 = Y3$ (as it happens on the transmitter's side with $X1 = X2 = X3$). The effect of errors can be generically modeled as $Y = X \oplus E$, where E is the error pattern [34]. In a situation without errors, $Y = X \oplus E = X$, and thus, $E = 0$. The presence of errors is analyzed in the receiver through XOR operations on the received characters $X1$, $X2$, and $X3$. These operations are performed by the hardware on $\{Y1, Y2, Y3\}$ as follows: $Z = (Y1 \oplus Y2) \oplus (Y1 \oplus Y3)$. If $Z = 0$, then the transmission errors are not present, or as will be analyzed further, there is a presence of a false error-free situation. Nonetheless, the EV battery charger must be ready to deal with this situation.

In the first case (a), the third bit of $X1$ is corrupted by an error, but because $Y2 = Y3$, then $Z = 0$, which means that $Y = X = 011, \ldots$. In this case, if the received RMS value is smaller than the previous value, the EV battery charger maintains the last value until it receives a new value. As seen further in the third example, this take of action from the EV battery charger is important to prevent overcurrent due to a false error-free situation. In the second case (b), all the characters are received without errors. The take of actions from the EV battery charger remains for an RMS value smaller than the previously received value. In the third case (c), all the characters are transmitted with the same error, and consequently, it is verified that the received characters are without errors. This

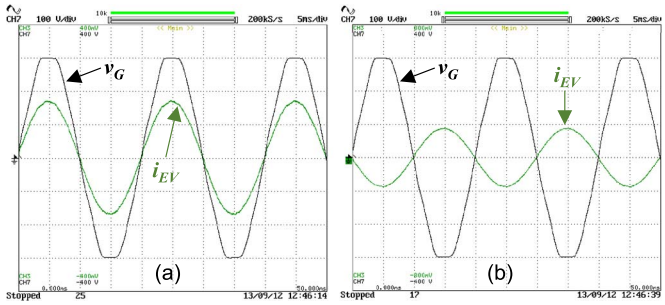

Fig. 10. Experimental results in steady state of the power grid voltage (v_G—100 V/div) and the EV battery charger current (i_{EV}—10 A/div) in (a) H2V operation mode and (b) V2G operation mode.

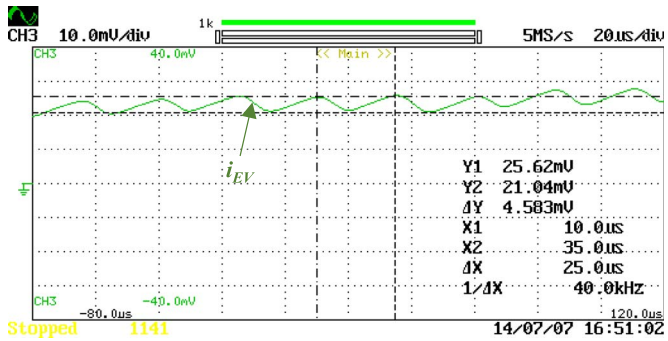

Fig. 11. Detail of the EV battery charger current ripple (1 A/div, 20 ms/div; for a switching frequency of 40 kHz).

is a case of a false error-free situation. In this case, if the RMS value is higher than the previously received value, the EV battery charger automatically decreases the current needed for charging the batteries. Otherwise, the EV battery charger must wait until it receives a new RMS value to confirm the absence of overcharge before increasing the current needed for charging the batteries. Without this "intelligent" action, the power grid current could exceed the maximum value contracted. It must be noted that, fortunately, this kind of errors is extremely rare [34]. In the last case (d), none of the characters are correctly received, and therefore, the error is easily detected, and the EV battery charger maintains the previous current reference.

V. Experimental Results

Several field tests were performed under realistic conditions to analyze the performance of the FIDPC in general and of the EV battery charger in particular. The EV battery charger is dedicated to charging lithium batteries; however, it can be used to charge any type of battery. The experimental results presented in this paper were obtained with a set of 24 sealed 12-V 33-Ah Absorbed Glass Mat batteries, connected in series to obtain a nominal voltage of 288 V and a capacity of 9.5 kWh. The results were registered with a *Yokogawa DL708E* digital oscilloscope, acquiring the signal at a sampling frequency of 1 kS/s. The voltage from the power grid was acquired and visualized before making the tests with the FIDPC. The voltage presents distortion in its waveform (in the maximum and minimum amplitudes), due to the great amount of nonlinear loads connected upstream of the home electrical switchboard under test. Additionally, the nonlinear loads inside the home also contribute to this voltage distortion. Nevertheless, in both operation modes (H2V and V2G), the current at the bidirectional EV battery charger is kept as a sinusoidal waveform, avoiding any contribution to the voltage distortion.

A. Steady-State Operation

The experimental results obtained with the developed prototype in steady-state operation are shown in Figs. 10–13. Fig. 10(a) shows the power grid voltage (v_G) and the EV battery charger current (i_{EV}) during the battery charging process (i.e., with the EV battery charger working in the H2V mode). Fig. 10(b) presents the same voltage and current (v_G and i_{EV}), when part of the energy previously stored in the batteries of the

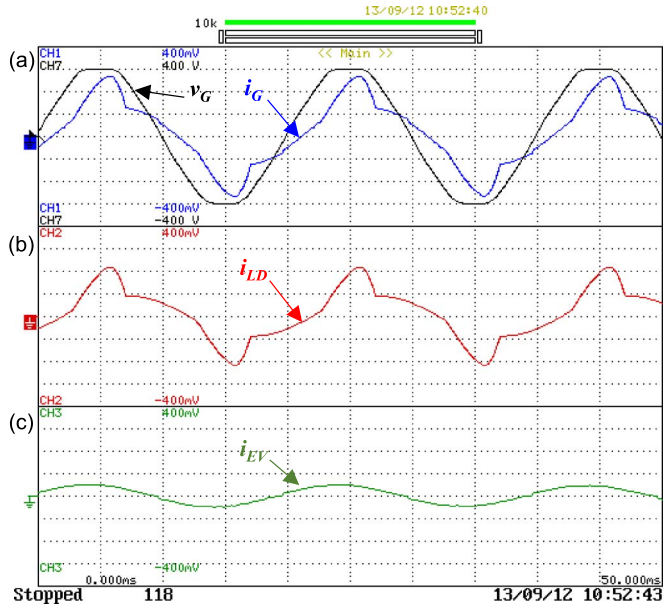

Fig. 12. Experimental results showing the EV battery charger in steady-state operation. (a) Power grid voltage (v_G—100 V/div) and grid current (i_G—10 A/div). (b) Home-load current (i_{LD}—10 A/div). (c) EV battery charger current (i_{EV}—10 A/div).

EV is delivered back to the power grid (EV battery charger in the V2G mode). Fig. 11 shows in detail the ac current ripple (0.5 A) and the switching frequency (40 kHz). A current with sinusoidal shape on the ac side of the EV battery charger can be observed, when working on both modes. This is an important contribution toward the preservation of power quality. In the H2V mode, the current is in phase with the voltage, whereas in the V2G mode, the phase turns by an angle of 180°, becoming in-phase opposition in relation to the voltage.

Fig. 12 shows the power grid voltage (v_G), the grid current (i_G), the home-load current (i_{LD}), and the EV battery charger current (i_{EV}). It is possible to observe in this last figure that the voltage is slightly distorted, whereas the current in the loads is highly distorted, and the EV battery charger current is sinusoidal.

Fig. 13 shows the spectral analysis and the $\mathrm{THD_i}\%$ of the grid current (i_G) for two cases: (a) with the EV battery charger working in H2V mode (i.e., with the EV batteries being charged) and (b) without the EV battery charger in operation.

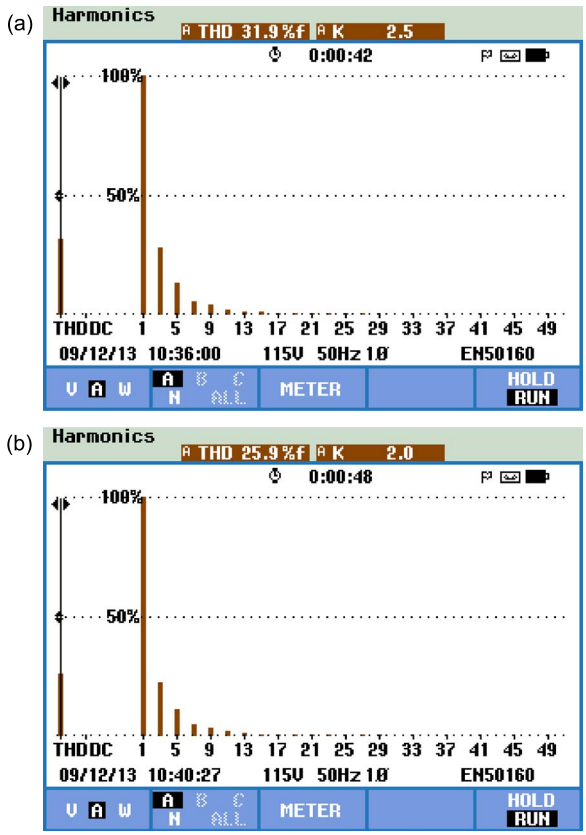

Fig. 13. Spectral analysis and THD% of the power grid current (i_G) in steady state. (a) Without the EV battery charger (THD% $= 31.9\%$). (b) With the EV battery charger working in H2V mode (THD% $= 25.9\%$).

A reduction of 6% (from 31.9% to 25.9%) was observed in the $\text{THD}_\text{i}\%$ of the grid current, when the EV battery charger was working and operating with sinusoidal current. These values were specific of the operating conditions, namely, the type of loads used, and, at the same time, of the sinusoidal charging current waveform at the EV battery charger. Undoubtedly, the fact that the EV battery charger contributes to preserving the power quality was observed and validated.

B. Transient Response

Fig. 14 shows the transient response of the EV battery charger as a function of a decrement in the home-load current. In this situation, the EV battery charger increases the charging current (i_{EV}). However, the absence of sudden variations in the current can also be observed, which is favorable for the power quality maintenance.

Fig. 15 shows the instantaneous values of the grid current (i_G), the home-load currents (i_{LD}), and the EV battery charger current (i_{EV}). This figure shows the transient response (during 100 s) of the EV battery charger as a function of several changes in the home-load current. In this case, the EV battery charger current (i_{EV}) is adjusted to a new value with a smooth response, after an elapse in the delay needed to calculate the RMS value of the home-load current (i_{LD}). As shown, the grid current (i_G) is kept almost constant and equal to 16 A. As shown in Fig. 15(b), the maximum current variation in the loads is 10 A.

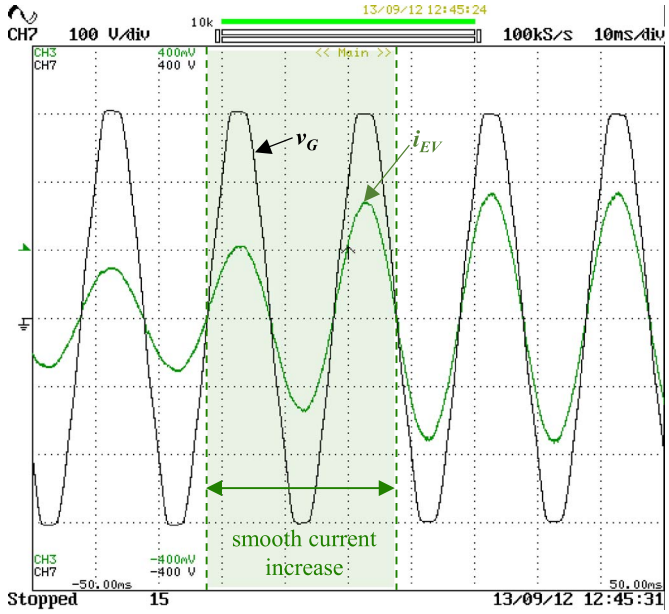

Fig. 14. Experimental results showing the power grid voltage (v_G—100 V/div) and the transient response of the EV battery charger current (i_{EV}—10 A/div) as a function of a decrement in the home-load current.

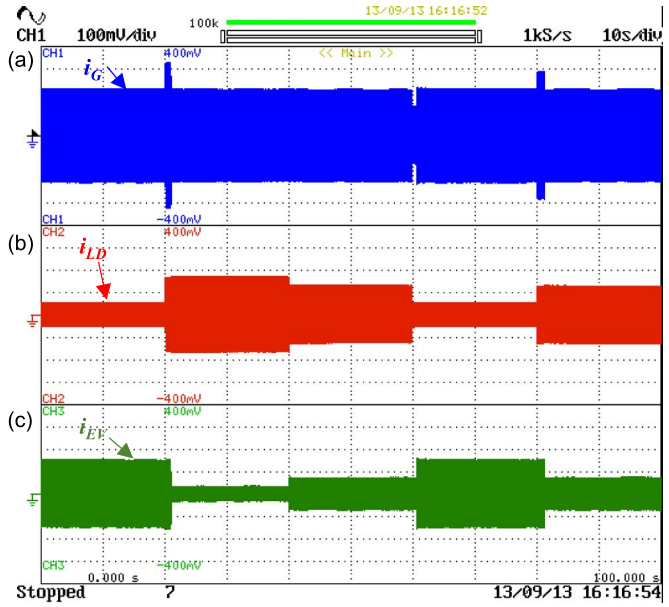

Fig. 15. Experimental results showing the transient response of the instantaneous values during several load variations in a short time interval of 100 s during the operation in H2V. (a) Grid current (i_G—10 A/div). (b) Home-load current (i_{LD}—10 A/div). (c) EV battery charger current (i_{EV}—10 A/div).

It is important to note that the grid current (i_G) reached 23 A for a very short period, which occurred during the delay to calculate the RMS value and further transmitted toward the EV battery charger. As circuit breakers usually operate by thermal losses, the RMS values of current above the nominal value (16 A in the presented case) are allowed during short periods of time without tripping. Fortunately, this means that higher values of currents during the RMS calculation delay can be easily accommodated by the circuit breaker of the home. Fig. 16 shows the one-cycle RMS values of the grid current (i_G), of the home-load current

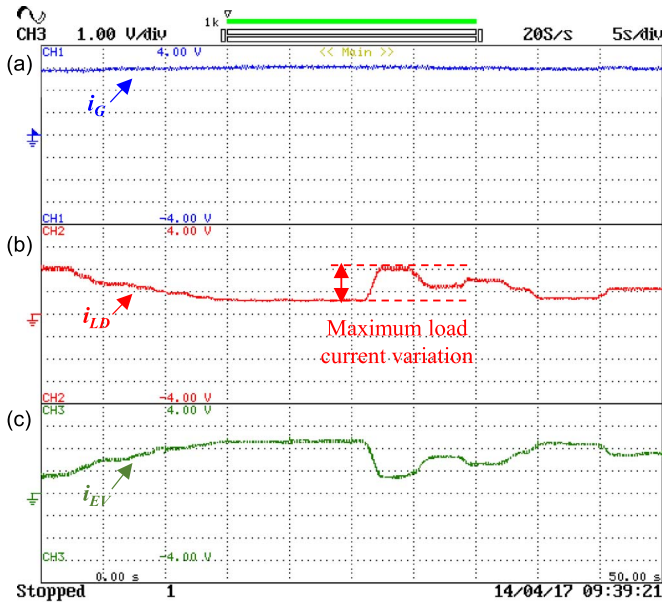

Fig. 16. Experimental results showing the transient response of the one-cycle RMS values of current during several load variations in a short time interval of 50 s during the operation in H2V mode. (a) Grid current (i_G—5 A/div). (b) Home-load current (i_{LD}—5 A/div). (c) EV battery charger current ($i_{\rm EV}$—5 A/div).

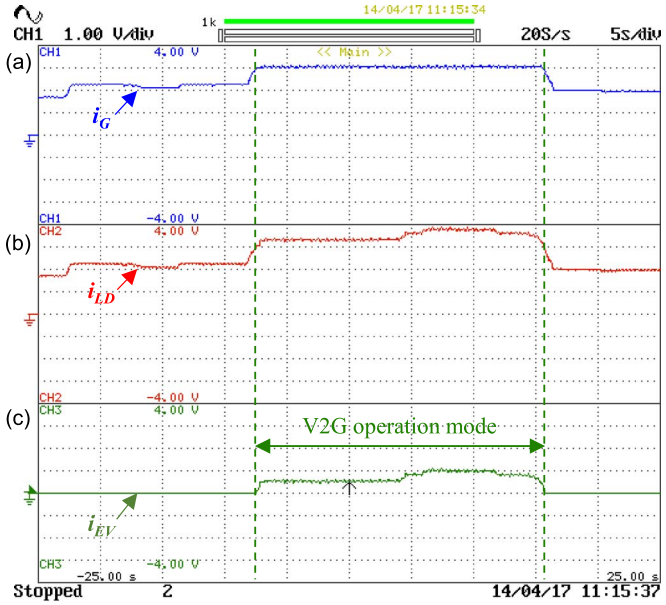

Fig. 17. Experimental results showing the transient response of the one-cycle RMS values during several load variations in a short time interval of 50 s and during the operation in V2G. (a) Grid current (i_G—5 A/div). (b) Home-load current (i_{LD}—5 A/div). (c) EV battery charger current ($i_{\rm EV}$—5 A/div).

(i_{LD}), and of the EV battery charger current ($i_{\rm EV}$). It can be observed in this figure that the controller of the EV battery charger adjusts the current with a smooth response, avoiding fast current variations that can be problematic to the electric installation. In this situation, the grid current was maintained almost constant and equal to 16 A, whereas the load current experienced a variation of 7 A.

As aforementioned, the EV can be used to provide energy to the power grid (V2G operation mode) due to its possibility of operating in bidirectional mode. Therefore, this operation mode can also be used to avoid trips in the circuit breaker when the home current exceeds the maximum allowed value that was specified. This situation is confirmed in Fig. 17. In this case, the EV is plugged in and not charged. The EV starts the operation as V2G, when the RMS value of the home-load current (i_{LD}) exceeds the maximum allowed. Consequently, it is also possible to confirm in Fig. 17(a) that the RMS value of the grid current (i_G) does not exceed the maximum current of the circuit breaker (16 A).

Fig. 18 shows the experimental results of the FIDPC transient response (200 s) during the H2V and V2G operation modes. Fig. 18(a) shows the dc-link voltage ($v_{\rm DC}$) and the current to charge the batteries (i_{BAT}). Fig. 18(b) shows the RMS value of the EV battery charger current. This result was registered to illustrate the beginning of the battery charging process, the adjusting of the charging current according to the aforementioned algorithms, and the beginning of the battery discharging process. According to this figure, in stage (1), the dc-link voltage ($v_{\rm DC}$) was controlled to its voltage reference (360 V) with energy provided by the EV batteries. After this stage, the EV battery charger was connected to the power grid, and the dc-link voltage ($v_{\rm DC}$) was controlled to a new reference value (400 V). Stage (2) starts when the dc-link voltage ($v_{\rm DC}$)

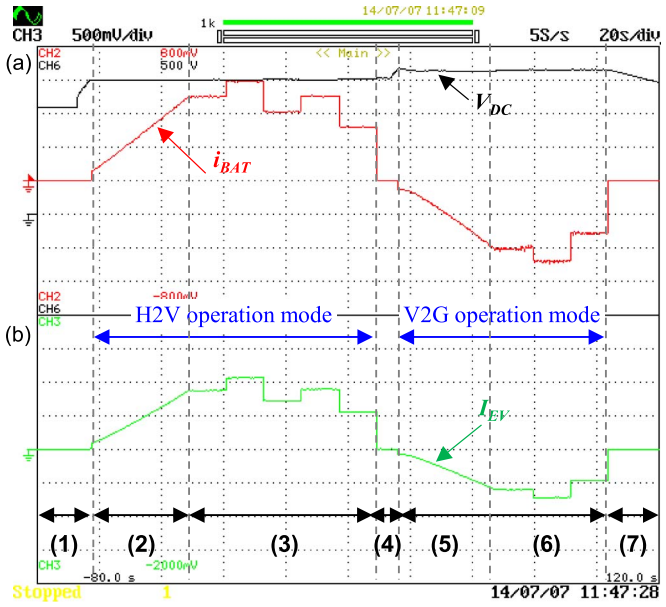

Fig. 18. Experimental results showing a transient response in a time interval of 200 s during H2V and V2G operation modes. (a) DC-link voltage ($v_{\rm DC}$—100 V/div) and battery charging current (i_{BAT}—2 A/div). (b) RMS value of the EV battery charger current ($i_{\rm EV}$—2 A/div).

reaches the new reference voltage. Then, the battery charging current (i_{BAT}) slowly increases. During stage (3), the battery charging current (i_{BAT}) was adjusted according to the FIDPC control algorithm. This last statement was the reason for the current variation during this stage. During stage (4), the battery charging process was interrupted, and the dc-link voltage was controlled to a new voltage reference (430 V). This higher voltage value in the dc link was necessary to achieve a sine-wave current on the ac side when delivering energy back to

the power grid. Stage (5) has initiated after the dc-link voltage (v_{DC}) reached the new voltage reference (430 V). In this fifth stage, the battery discharging current slowly increased. During stage (6), the battery discharge current was adjusted according to the FIDPC control algorithm. This explains why the battery discharge current was always changing along this entire stage. Finally, the V2G operation mode was stopped in stage (7).

C. Discussion

As expected, it is possible to confirm that the ac current in the EV battery charger is sinusoidal when the experimental results were taken in steady state during the H2V and V2G operation modes. Additionally and considering the H2V operation mode, it is possible to confirm that the EV battery charger is clearly able to adjust the current as a function of the RMS values received from the electrical switchboard through the RF communication. It is also important to note that the current waveform is not affected during the transient response, i.e., this current remains sinusoidal, and at the same time, the TPF is kept unitary. The proposed FIDPC was validated in a particular case, but it can be generalized to address this solution to a set of cases. For this purpose, it is enough to install an RF transmitter in the electrical switchboard where the EV is plugged. Therefore, the battery charging process of an EV can be controlled according to the power limits of the installation in which it is plugged.

VI. Conclusion

This paper has presented an FIDPC of battery chargers for EVs, which was designed taking into account the context of smart grids. An innovative strategy for dynamic power control of an EV battery charger was presented and associated to the proposed FIDPC. The developed prototype allows for the dynamic adjustment of the RMS value of the EV battery charger current in response to changes in the current required by the other loads of the home. The communication between the home electrical switchboard and the EV is supported by RF communication, which simplifies the installation process. The behavior of the EV battery charger prototype was evaluated through realistic conditions. Finally, it can be concluded that this FIDPC supported on RF communication is an interesting solution to be applied in smart homes, contributing to the reliability and expansion of smart grids.

References

[1] F. R. Salmasi, "Control strategies for hybrid electric vehicles: Evolution, classification, comparison, and future trends," *IEEE Trans. Veh. Technol.*, vol. 56, no. 5, pp. 2393–2404, Sep. 2007.

[2] S. S. Raghavan and A. Khaligh, "Electrification potential factor: Energy-based value proposition analysis of plug-in hybrid electric vehicles," *IEEE Trans. Veh. Technol.*, vol. 61, no. 3, pp. 1052–1059, Mar. 2012.

[3] A. Y. Saber and G. K. Venayagamoorthy, "Plug-in vehicles and renewable energy sources for cost and emission reductions," *IEEE Trans. Ind. Electron.*, vol. 58, no. 4, pp. 1229–1238, Apr. 2011.

[4] S. Gao, K. T. Chau, C. Liu, D. Wu, and C. C. Chan, "Integrated energy management of plug-in electric vehicles in power grid with renewables," *IEEE Trans. Veh. Technol.*, vol. 63, no. 7, pp. 3019–3027, Sep. 2014.

[5] F. Kennel, D. Görges, and S. Liu, "Energy management for smart grids with electric vehicles based on hierarchical MPC," *IEEE Trans. Ind. Informat.*, vol. 9, no. 3, pp. 1528–1537, Aug. 2013.

[6] A. Khaligh and Z. Li, "Battery, ultracapacitor, fuel cell, and hybrid energy storage systems for electric, hybrid electric, fuel cell, and plug-in hybrid electric vehicles: State of the art," *IEEE Trans. Veh. Technol.*, vol. 59, no. 6, pp. 2806–2814, Jul. 2010.

[7] E. Inoa and J. Wang, "PHEV charging strategies for maximized energy saving," *IEEE Trans. Veh. Technol.*, vol. 60, no. 7, pp. 2978–2986, Sep. 2011.

[8] N. Liu, J. Chen, L. Zhu, J. Zhang, and Y. He, "A key management scheme for secure communications of advanced metering infrastructure in smart grid," *IEEE Trans. Ind. Electron.*, vol. 60, no. 10, pp. 4746–4756, Oct. 2013.

[9] M. Basu, K. Gaughan, and E. Coyle, "Harmonic distortion caused by EV battery chargers in the distribution systems network and its remedy," in *Proc. Int. Conf. UPEC*, Jan. 2004, pp. 869–873.

[10] S. G. Wirasingha and A. Emdai, "Classification and review of control strategies for plug-in hybrid electric vehicles," *IEEE Trans. Veh. Technol.*, vol. 60, no. 1, pp. 111–122, Jan. 2011.

[11] J. A. P. Lopes, F. Soares, and P. M. R. Almeida, "Integration of electric vehicles in the electric power systems," *Proc. IEEE*, vol. 99, no. 1, pp. 168–183, Jan. 2011.

[12] T. Zhang, W. Chen, Z. Han, and Z. Cao, "Charging scheduling of electric vehicles with local renewable energy under uncertain electric vehicle arrival and grid power price," *IEEE Trans. Veh. Technol.*, vol. 63, no. 6, pp. 2600–2612, Jul. 2014.

[13] K. J. Dyke, N. Schofield, and M. Barnes, "The impact of transport electrification on electrical networks," *IEEE Trans. Ind. Electron.*, vol. 57, no. 12, pp. 3917–3926, Dec. 2010.

[14] J. J. Escudero-Garzás, A. García-Armada, and G. Seco-Granados, "Fair design of plug-in electric vehicles aggregator for V2G regulation," *IEEE Trans. Veh. Technol.*, vol. 61, no. 8, pp. 3406–3419, Oct. 2012.

[15] R. Smolenski, M. Jarnut, G. Benysek, and A. Kempski, "AC/DC/DC interfaces for V2G applications—EMC issues," *IEEE Trans. Ind. Electron.*, vol. 60, no. 3, pp. 930–935, Mar. 2013.

[16] M. D. Galus, S. Koch, and G. Andersson, "Provision of load frequency control by PHEVs, controllable loads, and a cogeneration unit," *IEEE Trans. Ind. Electron.*, vol. 58, no. 10, pp. 4568–4582, Oct. 2011.

[17] M. El Chehaly, O. Saadeh, C. Martinez, and G. Joos, "Advantages and applications of vehicle to grid mode of operation in plug-in hybrid electric vehicles," in *Proc. IEEE EPEC*, Oct. 2009, pp. 1–6.

[18] V. C. Gungor *et al.*, "Smart grid and smart homes—Key players and pilot projects," *IEEE Ind. Electron. Mag.*, vol. 6, no. 4, pp. 18–34, Dec. 2012.

[19] C. Liu, K. T. Chau, D. Wu, and S. Gao, "Opportunities and challenges of vehicle-to-home, vehicle-to-vehicle, and vehicle-to-grid technologies," *Proc. IEEE*, vol. 101, no. 11, pp. 2409–2427, Nov. 2013.

[20] C. Jin, J. Tang, and P. Ghosh, "Optimizing electric vehicle charging: A customer's perspective," *IEEE Trans. Veh. Technol.*, vol. 62, no. 7, pp. 2919–2927, Sep. 2013.

[21] D. Li and S. K. Jayaweera, "Distributed smart-home decision-making in a hierarchical interactive smart grid architecture," *IEEE Trans. Parallel Distrib. Syst.*, vol. 26, no. 1, pp. 75–84, Jan. 2015.

[22] D. Li and S. K. Jayaweera, "Machine-learning aided optimal customer decisions for an interactive smart grid," *IEEE Syst. J.*, vol. 9, no. 4, pp. 1529–1540, Dec. 2015.

[23] H. Turton and F. Moura, "Vehicle-to-grid systems for sustainable development: An integrated energy analysis," *Elsevier Technol. Forecast. Soc. Change*, vol. 75, no. 8, pp. 1091–1108, Oct. 2008.

[24] K. Clement-Nyns, E. Haesen, and J. Driesen, "The impact of charging plug-in hybrid electric vehicles on a residential distribution grid," *IEEE Trans. Power Syst.*, vol. 25. no. 1, pp. 371–380, Feb. 2010.

[25] Z. Shang, S. Cui, Q. Wang, H. Zhang, and W. Ge, "On applications of short distance RF for smart grid at distribution level," in *Proc. IEEE Int. Symp. Instrum. Meas., Sensor Netw. Autom.*, Dec. 2013, pp. 584–587.

[26] M. C. Kisacikoglu, B. Ozpineci, and L. M. Tolbert, "Examination of a PHEV bidirectional charger system for V2G reactive power compensation," in *Proc. IEEE APEC*, Feb. 2010, pp. 458–465.

[27] S. Han, S. Han, and K. Sezaki, "Development of an optimal vehicle-to-grid aggregator for frequency regulation," *IEEE Trans. Smart Grid*, vol. 1, no. 1, pp. 65–72, Jun. 2010.

[28] J. Martins, F. P. Brito, D. Pedrosa, V. Monteiro, and J. L. Afonso, "Real-life comparison between diesel and electric car energy consumption," in *Grid Electrified Vehicles: Performance, Design and Environmental Impacts*, 1st ed., C. A. M. da Silva, Ed. Commack, NY, USA: Nova, 2013, ch. 10, pp. 209–232.

[29] J. C. Ferreira, A. Silva, V. Monteiro, and J. L. Afonso, "Collaborative broker for distributed energy resources," in *Computational Intelligence and Decision Making*, 1st ed., A. Madureira, C. Reis, and V. Marques, Eds. Dordrecht, The Netherlands: Springer-Verlag, 2013, pp. 367–378.

[30] A. A.-H. Hussein and I. Batarseh, "A review of charging algorithms for nickel and lithium battery chargers," *IEEE Trans. Veh. Technol.*, vol. 60, no. 3, pp. 830–838, Mar. 2011.
[31] Lithium Battery Datasheet WB-LYP90AHA Charge and Discharge Chart, Winston Battery, Shenzhen, China, Jan. 2007.
[32] M. Karimi-Ghartemani, "Linear and Pseudolinear Enhanced Phased-Locked Loop (EPLL) structures," *IEEE Trans. Ind. Electron.*, vol. 61, no. 3, pp. 1464–1474, Mar. 2014.
[33] S. Orts-Grau, F. J. Gimeno-Sales, A. Abellan-Garcia, S. Segui-Chilet, and J. C. Alfonso-Gil, "Improved shunt active power compensator for IEEE standard 1459 compliance," *IEEE Trans. Power Del.*, vol. 25, no. 4, pp. 2692–2701, Oct. 2010.
[34] A. B. Carlson, *Communication Systems: An Introduction to Signals and Noise in Electrical Communication*, 4th ed. New York, NY, USA: McGraw-Hill, 2002.

Vítor Monteiro (S'10) was born in Guimarães, Portugal, in May 1984. He received the M.Sc. degree in industrial electronics and computer engineering from the University of Minho, Guimarães, in 2012, where he is currently working toward the Ph.D. degree.

Since 2008, he has been a member of the Group of Energy and Power Electronics (GEPE) and a collaborator with Centro Algoritmi, University of Minho. His research interests include power electronic converters, digital control techniques, smart grids, and electric vehicles.

Mr. Monteiro received a Doctoral Scholarship from the Foundation for Science and Technology of Portugal.

João Paulo Carmo was born in Maia, Portugal, in 1970. He received the B.S. and M.Sc. degrees in electrical engineering from the University of Porto, Porto, Portugal, in 1993 and 2002, respectively, and the Ph.D. degree in industrial electronics from the University of Minho, Guimarães, Portugal, in 2007.

Since 2014, he has been a Professor with the University of São Paulo (USP), São Paulo, Brazil. He is also the Vice Director of the Metamaterials–Microwaves and Optics Group, USP, and a collaborator with the MEMS-UMinho (MicroElectroMechanical Systems) R&D Center, University of Minho. His research interests include micro/nanofabrication technologies for mixed-mode/radio frequency and optic systems, solid-state integrated sensors, microactuators, and micro/nanodevices for use in biomedical and industrial applications.

J. G. Pinto (M'14) was born in Guimarães, Portugal, in 1977. He received the B.Sc. degree in electronics engineering, the M.Sc. degree in industrial electronics, and the Ph.D. degree in electronics and computer engineering from the University of Minho, Guimarães, Portugal, in 2001, 2004, and 2012, respectively.

From 2002 to 2006, he was an invited Assistant Lecturer with the Department of Electrical Engineering, Polytechnic Institute of Bragança, Bragança, Portugal. From 2006 to 2012, he was a Researcher with the Group of Energy and Power Electronics (GEPE), Centro Algoritmi, University of Minho. Since 2013, he has been an invited Assistant Professor with the Department of Industrial Electronics, University of Minho. His research interests include power electronics, power quality, and digital control of power converters.

João Luiz Afonso (M'00) was born in Rio de Janeiro, Brazil, in 1963. He received the B.S. and M.Sc. degrees in electrical engineering from the Federal University of Rio de Janeiro, in 1986 and 1991, respectively, and the Ph.D. degree in industrial electronics from the University of Minho, Guimarães, Portugal, in 2000.

Since 1993, he has been with the Department of Industrial Electronics, University of Minho, where he is currently an Associate Professor. He teaches electrical machines, electrical energy systems, complements of power electronics, electrical power quality, active power filters, and renewable energy. He is a Researcher with the Group of Energy and Power Electronics (GEPE) and coordinates the thematic strand of Sustainable and Smart Cities of the Centro Algoritmi. His research interests include power quality, active power filters, renewable energy, electric vehicles, energy efficiency, energy storage systems, smart grids, and smart cities.